


# Anisotropic photogalvanic effects in monolayer $WSe_2$ under elliptically polarized light

Jinyan Niu(牛金艳), Yonghong Ma(马永红), Wuming Liu(刘伍明), and Jia Liu(刘佳)
**Citation:**Chin. Phys. B, 2026, 35 (**7**): 077302. DOI: 10.1088/1674-1056/ae7a06
http://cpb.iphy.ac.cn; http://iopscience.iop.org/cpb

**What follows is a list of articles you may be interested in**

---

## Ultra-high anisotropy and electronic property of two-dimensional $PbSnS_2$ with a black phosphorus structure

Xinlong Wang(王鑫龙), Shihao Wang(王诗皓), Yandi Jiang(姜彦迪), Qing Min(闵清), Haiming Huang(黄海铭), Chengrui Wu(吴承瑞), and Juntao Yang(杨俊涛)
Chin. Phys. B, 2026, 35 (**5**): 057304. DOI: 10.1088/1674-1056/ae1568

## In-plane optical anisotropy of InGaN/GaN quantum disks in nanowires investigated by reflectance difference spectroscopy

Tingting Wei(韦婷婷), Jinling Yu(俞金玲), Zhu Diao, Zhaonan Li(李兆男), Shuying Cheng(程树英), Yunfeng Lai(赖云锋), Yonghai Chen(陈涌海), and Chao Zhao(赵超)
Chin. Phys. B, 2025, 34 (**6**): 067302. DOI: 10.1088/1674-1056/adc6f4

## Nonlinear current response and electric quantum oscillations in the Dirac semimetal $Cd_3As_2$

Hao-Nan Cui(崔浩楠), Ze-Nan Wu(吴泽南), Jian-Kun Wang(王建坤), Guang-Yu Zhu(祝光宇), Jia-Jie Yang(杨佳洁), Wen-Zhuang Zheng(郑文壮), Zhi-Min Liao(廖志敏), Shuo Wang(王硕), Ben-Chuan Lin(林本川), and Dapeng Yu(俞大鹏)
Chin. Phys. B, 2023, 32 (**8**): 087306. DOI: 10.1088/1674-1056/acd9c5

## Room temperature quantum anomalous Hall insulator in honeycomb lattice, $RuCS_3$, with large magnetic anisotropy energy

Yong-Chun Zhao(赵永春), Ming-Xin Zhu(朱铭鑫), Sheng-Shi Li(李胜世), and Ping Li(李萍)
Chin. Phys. B, 2023, 32 (**5**): 057301. DOI: 10.1088/1674-1056/aca396

## Single-layer intrinsic 2H-phase $LuX_2$ ($X$ = Cl, Br, I) with large valley polarization and anomalous valley Hall effect

Chun-Sheng Hu(胡春生), Yun-Jing Wu(仵允京), Yuan-Shuo Liu(刘元硕), Shuai Fu(傅帅),Xiao-Ning Cui(崔晓宁), Yi-Hao Wang(王易昊), and Chang-Wen Zhang(张昌文)
Chin. Phys. B, 2023, 32 (**3**): 037306. DOI: 10.1088/1674-1056/ac89d6

---

# Anisotropic photogalvanic effects in monolayer $WSe_2$ under elliptically polarized light

Jinyan Niu(牛金艳)[1], Yonghong Ma(马永红)[1], Wuming Liu(刘伍明)[1,2,†], and Jia Liu(刘佳)[1,‡]

[1] *School of Science, Inner Mongolia University of Science and Technology, Baotou* 014010, *China*

[2] *Beijing National Laboratory for Condensed Matter Physics, Institute of Physics, Chinese Academy of Sciences, Beijing* 100080, *China*

(Received 9 April 2026; revised manuscript received 8 June 2026; accepted manuscript online 9 June 2026)

We investigate the photogalvanic effect in monolayer $WSe_2$ under elliptically polarized light using non-equilibrium Green's function density functional theory (NEGF-DFT) simulations. When defects are added that reduce the intrinsic $D_{3h}$ symmetry to $C_s$ and $C_{2v}$, the photocurrent shows distinct direction-dependent responses: a sine function of the helicity angle along the zigzag direction and a cosine function along the armchair direction. This anisotropy arises from the specific nonzero tensor elements activated by symmetry reduction. Ga substitution is identified as a highly effective strategy, enhancing the polarization sensitivity by 55.54 times compared to that of pristine $WSe_2$. Furthermore, we reveal a resonant enhancement mechanism via impurity states introduced by Ga doping, as confirmed by projected density of states (PDOS) analysis. The application of a small bias voltage (0.04 V) further boosts the photocurrent by up to 368 times. These findings establish a direct link between crystal symmetry, defect engineering, and photoresponse, providing a pathway for high-performance polarization-sensitive optoelectronic devices.

**Keywords:** photogalvanic effects, monolayer $WSe_2$, anisotropy, defect

**PACS:** 73.50.Pz, 73.63.–b, 78.67.–n, 72.10.–d

**DOI:** 10.1088/1674-1056/ae7a06 **CSTR:** 32038.14.CPB.ae7a06

## 1. Introduction

The photogalvanic effect (PGE)[1–3] is a unique photoelectric phenomenon that occurs in devices lacking spatial inversion symmetry.[4–8] When valence-band electrons in a semiconductor absorb photons, they not only transition to the conduction band to form electron–hole pairs but also gain sufficient energy to escape the nucleus and become free electrons. Furthermore, when illuminated with polarized light, the transition of excited electrons from the valence band can generate a continuous photocurrent,[9,10] ultimately converting light energy into electrical energy.

The core function of the PGE is to efficiently separate and utilize photogenerated carriers. In optoelectronic devices, it can overcome the limitations of traditional carrier separation methods. Although conventional p–n junctions can separate free electrons and holes via an electric field to generate photocurrent,[11–13] their performance is constrained by the Shockley–Queisser (S–Q) limit,[14] making it difficult to further enhance device efficiency. In contrast, the mechanism of the PGE utilizes the momentum-space distribution of nonequilibrium carriers (driven by symmetry breaking) rather than the thermal equilibrium diffusion mechanism of a conventional p–n junction. Since the PGE does not depend on the diffusion length of minority carriers and can generate a huge photocurrent under specific bias in certain two-dimensional (2D) monolayer devices, some energy conversion efficiency metrics (such as the responsivity under specific polarization) can surpass the limitations of the traditional S–Q limit. Additionally, the PGE can generate sustained photocurrent under polarized light excitation, providing critical support for improving photocurrent response efficiency and breaking through performance bottlenecks in optoelectronic devices.[4–10]

The development of current optoelectronic devices faces a fundamental performance bottleneck: conventional p–n junction-based devices are limited by the S–Q limit,[14] which restricts further improvements in carrier separation efficiency and photocurrent response capability, making it impossible to meet the demands of high-precision and high-sensitivity applications. The PGE offers unique advantages — it can directly generate photocurrent in devices without spatial inversion symmetry[4–8] and produce sustained photocurrent under polarized light illumination.[9,10] These properties enable the PGE to overcome the performance constraints of traditional structures, providing a new pathway to address issues such as low efficiency and limited performance in optoelectronic devices. Therefore, in-depth research into the PGE is urgently needed.

Research into the PGE has significant theoretical value and practical application importance. Theoretically, it advances our understanding of carrier transition and separation mechanisms in semiconductors, particularly in the study of photoelectric processes in low-dimensional materials (e.g., 2D

†Corresponding author. E-mail: wmliu@iphy.ac.cn

‡Corresponding author. E-mail: jialiu@imust.edu.cn

© 2026 Chinese Physical Society and IOP Publishing Ltd. All rights, including for text and data mining, AI training, and similar technologies, are reserved.

materials and quantum wells), thereby enriching the fundamental theoretical framework of photoelectronics.[15–27] Practically, the broad application potential of the PGE in various fields, such as electron gas,[15–18] atoms,[19] semiconductor quantum wells,[20,21] 2D perovskites,[22] topological insulators,[23,24] and Weyl semimetals,[25–27] provides core technological support for developing novel high-efficiency optoelectronic devices (e.g., high-sensitivity photodetectors and high-conversion-efficiency solar cells). This research can help the optoelectronics industry overcome performance limitations and drive technological innovation in energy and sensing applications.

Transition-metal dichalcogenides (TMDCs) are inorganic compounds with layered structures[28–30] held together by van der Waals forces. Consequently, methods similar to those used for graphene can be employed to separate TMDC blocks into single- or multilayer nanosheets.[31–37] As the number of layers decreases, TMDCs exhibit interesting layer-dependent properties, such as excellent bandgap characteristics and high carrier mobility, which are attributed to quantum constraints and surface effects.[38–40] In experiments and applications, the choice of materials depends on whether large crystals can be synthesized easily and whether doping behavior can be adjusted. Despite the fact that tungsten diselenide ($WSe_2$) has recently attracted significant attention in the field of semiconductors,[41–44] the influence of the PGE on anisotropic $WSe_2$ has not been sufficiently investigated. $WSe_2$ has $D_{3h}$ symmetry and breaks space inversion symmetry, inducing the PGE effect. However, the magnitude of the photocurrent is usually very low, limiting the efficiency of light conversion into current and its subsequent practical application. Theoretical and experimental results have shown that if we can reduce the symmetry of the device, we can enhance the strength of the photocurrent, and this symmetry adjustment can be achieved by defects,[45] strains,[46,47] and the construction of heterogeneous structures.[11,13]

In this paper, we systematically study a 2D $WSe_2$ photodetector under full-range visible elliptically polarized light, considering transport directions (zigzag/armchair) and defect types (vacancy and substitution). Figure 1 shows the monolayer $WSe_2$ photodetector, where orange and blue points represent Se and W atoms, respectively; the lattice constant is 3.327 Å, and the W–Se, W–W, and Se–Se bond lengths are 2.553 Å, 3.327 Å, and 3.362 Å, respectively. Figures 1(a) and 1(b) present top/side views of the zigzag-direction device ($x$: transport, $y$: periodic), while Figs. 1(e) and 1(f) show those of the armchair-direction device ($x$: periodic, $y$: transport). Dashed lines at both ends separate the central region (39 atoms for the zigzag device, 30 for the armchair device) from infinite left/right leads. Vertical light incident on the central $x$–$y$ plane is shown in Figs. 1(b) and 1(f), and a 20 Å vacuum layer is used to avoid interlayer interaction. Six configurations are discussed: pure $WSe_2$, Ga, S, and Te substitutes, and Se/W vacancies. Figures 1(c) and 1(g) illustrate W-vacancy/Ga-substituted configurations for the zigzag/armchair directions, while Figs. 1(d) and 1(h) show the Se-vacancy or S/Te-substituted configurations of the zigzag/armchair directions, respectively. The dotted red boxes in Figs. 1(b) and 1(f) indicate that the defects appear in the middle of the central region. The $D_{3h}$ symmetry of the pristine $WSe_2$ monolayer is reduced to $C_s$ and $C_{2v}$ due to defect-induced inversion symmetry breaking.

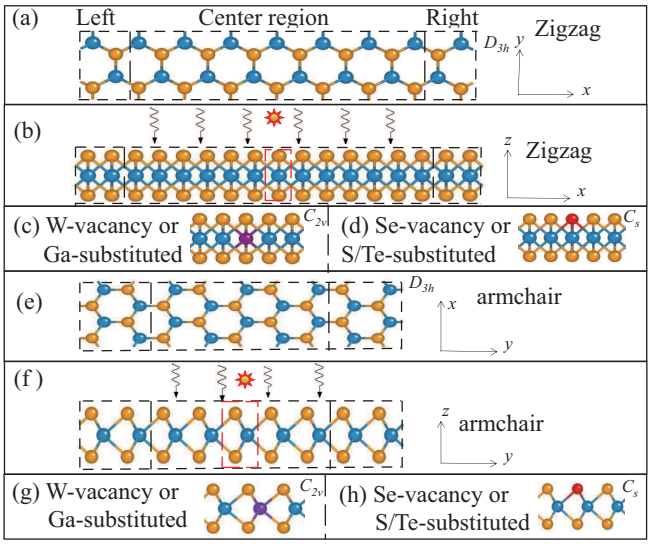



**Fig. 1.** (a) Top and (b) side views of a monolayer $WSe_2$ photodetector based on the zigzag configuration. (e) Top and (f) side views of a monolayer $WSe_2$ photodetector based on the armchair configuration. Blue: W, orange: Se, purple: Ga, red: S/Te. (c)/(g) W-vacancy or Ga-substituted configurations in zigzag/armchair devices, (d)/(h) Se-vacancy or S/Te-substituted configurations in zigzag/armchair devices.

## 2. Computational methods

The elliptic photogalvanic effect (EPGE) occurs when the central region is irradiated by elliptically polarized light. The excited electrons jump from the valence band to the conduction band and generate a constant photocurrent under the control of the built-in electric field. The photocurrent $J_{\mathrm{L}}^{(\mathrm{ph})}$ of the left lead takes the following form:[3]

$$J_{\mathrm{L}}^{(\mathrm{ph})} = \frac{ie}{h}\int \mathrm{Tr}\{\Gamma_{\mathrm{L}}[G^{<(\mathrm{ph})} + f_{\mathrm{L}}(E)(G^{>(\mathrm{ph})} - G^{<(\mathrm{ph})})]\}\mathrm{d}E, \quad (1)$$

where i is the imaginary unit, $e$ is the electronic charge, $h$ is Planck's constant, $\Gamma_{\mathrm{L}}$ describes the coupling between the scattering region and the left electrode, and $f_{\mathrm{L}}$ is the Fermi–Dirac distribution function of the left electrode. $G^{>/<(\mathrm{ph})}$ denotes the greater/lesser Green's function with electron–photon interaction, which depends on symmetry, photon frequency, and polarization vector. When elliptically polarized light is incident upon the central region, the photocurrent is given by

$$J_{\mathrm{L}}^{(\mathrm{ph})} = \frac{ie}{h}\int \Big\{\cos^2\varphi \mathrm{Tr}\Big\{\Gamma_{\mathrm{L}}[G_1^{<(\mathrm{ph})} + f_{\mathrm{L}}(G_1^{>(\mathrm{ph})} - G_1^{<(\mathrm{ph})})]\Big\} + \sin^2\varphi \mathrm{Tr}\Big\{\Gamma_{\mathrm{L}}\Big[G_2^{<(\mathrm{ph})} + f_{\mathrm{L}}(G_2^{>(\mathrm{ph})} - G_2^{<(\mathrm{ph})})\Big]\Big\}$$

$$+\frac{\sin(2\varphi)}{2}\mathrm{Tr}\left\{\Gamma_{\mathrm{L}}\left[G_3^{<(\mathrm{ph})}+f_{\mathrm{L}}(G_3^{>(\mathrm{ph})}-G_3^{<(\mathrm{ph})})\right]\right\}\Big\}\mathrm{d}E, \tag{2}$$

where

$$\begin{aligned}
G_1^{>/<(\mathrm{ph})} &= \sum_{\alpha,\beta=x,y,z} \mathrm{C}_0 N G_0^{\mathrm{r}} e_{1\alpha} p_\alpha^+ G_0^{>/<} e_{1\beta} p_\beta G_0^\alpha,\\
G_2^{>/<(\mathrm{ph})} &= \sum_{\alpha,\beta=x,y,z} \mathrm{C}_0 N G_0^{\mathrm{r}} e_{2\alpha} p_\alpha^+ G_0^{>/<} e_{2\beta} p_\beta G_0^\alpha,\\
G_3^{>/<(\mathrm{ph})} &= \pm\mathrm{i}\sum_{\alpha,\beta=x,y,z}\sum_{j=1,2} \mathrm{C}_0 N\left(G_0^{\mathrm{r}} e_{j\alpha} p_\alpha^+ G_0^{>/<} e_{j\beta} p_\beta G_0^\alpha\right).
\end{aligned} \tag{3}$$

Here, $G_0^{\mathrm{r/a}}$ and $G_0^{>/<}$ correspond to the retarded/advanced and greater/lesser Green's functions, respectively, without photons, while $e_{1/2x,y,z}$ represents the Cartesian component of the unit vector $\boldsymbol{e}_{1(2)}$ determined by the polarization of light, and $p_{x,y,z}$ is the Cartesian component of the electron momentum. For elliptically polarized light, the polarization vector is given by $\boldsymbol{e}=\cos\varphi\boldsymbol{e}_1\pm\mathrm{i}\sin\varphi\boldsymbol{e}_2$, where "±" denotes right/left-handed elliptically polarized light, and $\varphi$ determines its helicity, e.g., $\varphi=\pm45^\circ$ corresponds to right- and left-handed circularly polarized light, respectively. In Eq. (3), $\mathrm{C}_0=\frac{e^2\hbar\sqrt{\mu_{\mathrm{r}}\varepsilon_{\mathrm{r}}}}{2Nm_0^2\omega\varepsilon C}I_\omega$, where $\mu_{\mathrm{r}}$ is the relative magnetic susceptibility, $\varepsilon$ ($\varepsilon_{\mathrm{r}}$) is the dielectric (relative dielectric) constant, $N$ is the number of photons, $\mathrm{m}_0$ is the bare electron mass, $\omega$ is the photon frequency, $C$ is the speed of light, and $I_\omega$ is the photon flux determined by the number of photons per unit area per unit time. The photoresponse function can be written as $R=J_{\mathrm{L}}^{(\mathrm{ph})}/eI_\omega$. Here, $R$ in units of $a_0^2$/phonon has the dimensions of area, where $a_0$ is the Bohr radius.

The non-equilibrium Green's function (NEGF) technique combined with density functional theory (DFT) is implemented in Nanoacademic Device Calculator (NanoDCAL),[48] and double-zeta atomic orbital bases with polarization functions are used to expand all physical quantities. The local density approximation is used to predict interchange and correlation phenomena. Atomic cores are defined by the standard norm conserving nonlocal pseudopotentials. The cutoff energy is 80 Hartree. $k$-point meshes of $10\times1\times1$ and $1\times10\times1$ are employed when calculating the photocurrent transport from the left probe to the right one.

## 3. Photocurrent and PDOS

The $WSe_2$ monolayer is a direct semiconductor with a bandgap of 1.532 eV.[49] Both the pure and the defective $WSe_2$ monolayers induce PGEs and generate photocurrent under vertical irradiation of elliptically polarized light, as shown in Fig. 2. To systematically explore the polarization-angle-dependent photoresponse, we deliberately select three typical photon energies of 2.6 eV (black line), 2.8 eV (red line), and 3.0 eV (blue line). These energies correspond to distinct interband transition regions along characteristic band dispersions, which can accurately reflect the law governing the evolution of the photoresponse under different excitation conditions. Six configurations are examined: (a) pure $WSe_2$, (b) W-vacancy, (c) Ga-substituted, (d) Se-vacancy, (e) S-substituted, and (f) Te-substituted. Due to the lack of spatial inversion symmetry, a photocurrent is generated even in the absence of a bias voltage. In the zigzag devices (left column), the photoresponse varies according to $\sin(2\varphi)$, consistent with the prediction $R_x\propto E_0^2\gamma_{xxz}\sin(2\varphi)$. Here, $E_0$ is the electric field intensity of the light and $\gamma_{xxz}$ is a tensor.[50] The maximum photocurrent occurs at $\varphi=45^\circ$ or $\varphi=135^\circ$, corresponding to right- and left-handed circularly polarized light, respectively. In the armchair devices (right column), the photocurrent varies according to $\cos(2\varphi+\delta\varphi)+C$, where $\delta\varphi$ and $C$ denote the phase shift and a constant that depends on the photon energy, respectively.[2] The maximum photocurrent is observed at $\varphi=0^\circ$ or $\varphi=90^\circ$, and it varies with the photon energy.

The distinct angular dependence of the photocurrent is dictated by the reduced point group symmetry induced by defects. In the zigzag devices, the symmetry is reduced to $C_s$ (characterized by a single mirror plane $\sigma_{xz}$). Group theory analysis reveals that this symmetry permits a photogalvanic tensor component $\gamma_{xxz}$, leading to a photocurrent response proportional to $\sin(2\varphi)$. Conversely, the armchair devices exhibit $C_{2v}$ symmetry (retaining two vertical mirror planes). This higher (reduced) symmetry allows for a different tensor configuration, specifically enabling a $\gamma_{yyz}$-dominated process. Consequently, the photocurrent follows a $\cos(2\varphi)$ dependence. This formal connection between the point group ($C_s$ vs. $C_{2v}$) and the specific nonvanishing tensor elements provides the fundamental physical mechanism underlying the observed anisotropic PGEs.

The photoresponses of $WSe_2$ devices show significant anisotropy: zigzag devices exhibit a sinusoidal dependence on helicity (peaks at $45^\circ/135^\circ$), while armchair devices show a cosinelike trend (peaks at $0^\circ/90^\circ$). Defects and photon energy further modulate these responses, demonstrating the tunability of PGEs in $WSe_2$.

To explore how photon energy, defect engineering, and crystal orientation jointly regulate the PGE in $WSe_2$, we investigate the maximum photocurrent $R_{\max}$ in devices with zigzag (Fig. 1(a)) and armchair (Fig. 1(b)) edges, covering six configurations: pure $WSe_2$ (black line), W-vacancy (red line), Ga-substituted (blue line), Se-vacancy (magenta line), S-substituted (green line), and Te-substituted (orange line). Below the $WSe_2$ bandgap (1.5 eV), the maximum photocurrent produced via the PGE is negligible, as photons lack the energy required to excite carriers. Above the bandgap, $R_{\max}$ varies nonlinearly, reflecting complex carrier dynamics. In zigzag devices, the S-substituted photodetector reaches $R_{\max}$ under ir-

radiation by elliptically polarized light, which is 5.63 at a photon energy of 2.5 eV. The $R_{max}$ of pure $WSe_2$ is 5.22 at 2.8 eV, while that of Te-substituted $WSe_2$ is 3.75 at 2.6 eV.[49] Figure 3(b) shows that for armchair devices, pure $WSe_2$ achieves the lowest photocurrent under irradiation by elliptically polarized light, and the Ga-substituted $WSe_2$ achieves a remarkable $R_{max}$ of 3.95 at 2.6 eV (55.54 times that of pure $WSe_2$), while other defects lead to smaller values of $R_{max}$ (mostly $< 2.4$). Consequently, it can be suggested that the photocurrent has obvious anisotropy, and the effect of defects on the elliptically polarized photocurrent is more significant in devices with armchair edges. In Ga-substituted case, the tuning of valley polarization and carrier mobility along the armchair direction enhances the photogalvanic response, showing that defects impact elliptically polarized photocurrent more in armchair-edged structures.

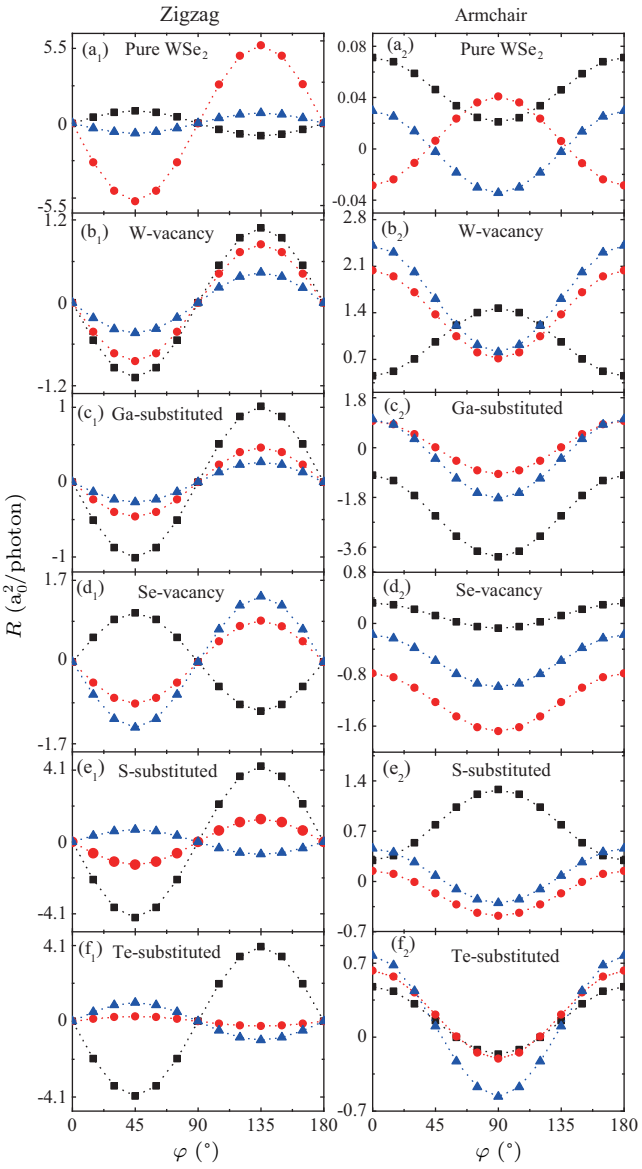



**Fig. 2.** Variation of the photoresponses of the zigzag (left column) and armchair (right column) devices with helicity $\varphi$ for photon energies of 2.6 eV (black line), 2.8 eV (red line), and 3.0 eV (blue line). (a) Pure $WSe_2$, (b) W-vacancy, (c) Ga-substituted, (d) Se-vacancy, (e) S-substituted, and (f) Te-substituted configurations.

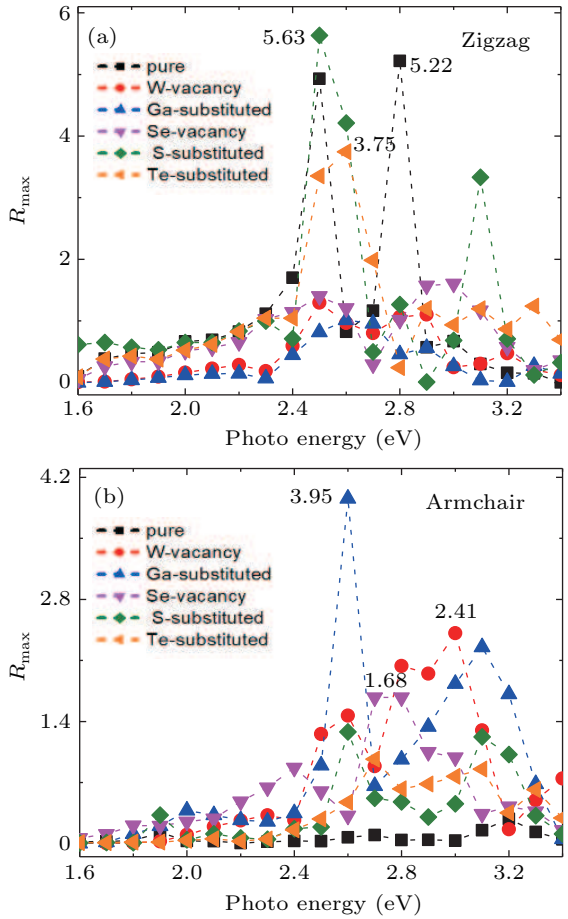



**Fig. 3.** Influence of photon energy on the maximum photocurrent ($R_{max}$) in devices with zigzag (a) and armchair (b) edges. Curves correspond to different configurations: pure $WSe_2$ (black line), W-vacancy (red line), Ga-substituted (blue line), Se-vacancy (magenta line), S-substituted (green line), and Te-substituted (orange line).

Since Ga doping exhibits the most pronounced photocurrent response along the armchair direction, we analyze its physical mechanism using the density of states as shown in Fig. 4: (a) original cell, Ga-substituted in (b) zigzag, and (c) armchair configurations. The three curves correspond to the s (black line), p (red line), and d (blue line) orbital densities of states based on the electronic localized landscape projection.

Comparing the projected densities of states (PDOSs) of a pristine $WSe_2$ nanoribbon and a Ga-doped configuration clearly reveals the remarkable modulation effect of Ga doping on electronic structure, which fundamentally accounts for the enhanced photocurrent and polarization sensitivity. In the case of the pristine $WSe_2$ nanoribbon, the valence and conduction bands are primarily contributed by the d orbitals of W atoms, followed by the p orbitals of Se atoms, while the contribution of s orbitals is nearly negligible. The Fermi level is located at the mid-gap position, and the density of states around the Fermi level is extremely low, resulting in insufficient carrier concentration and unfavorable conditions for the generation and transport of photogenerated carriers. After Ga atoms are substituted for W atoms, the electronic structure is effectively modulated. The pronounced enhancement of the

p-orbital density of states indicates strong orbital hybridization between Ga p orbitals and the adjacent orbitals of W and Se atoms, which plays a critical role in tuning the electronic structure. Meanwhile, the Fermi level clearly shifts toward the valence band, indicating strong p-type doping. The increased density of states near the Fermi level provides sufficient transport channels for photogenerated carriers.

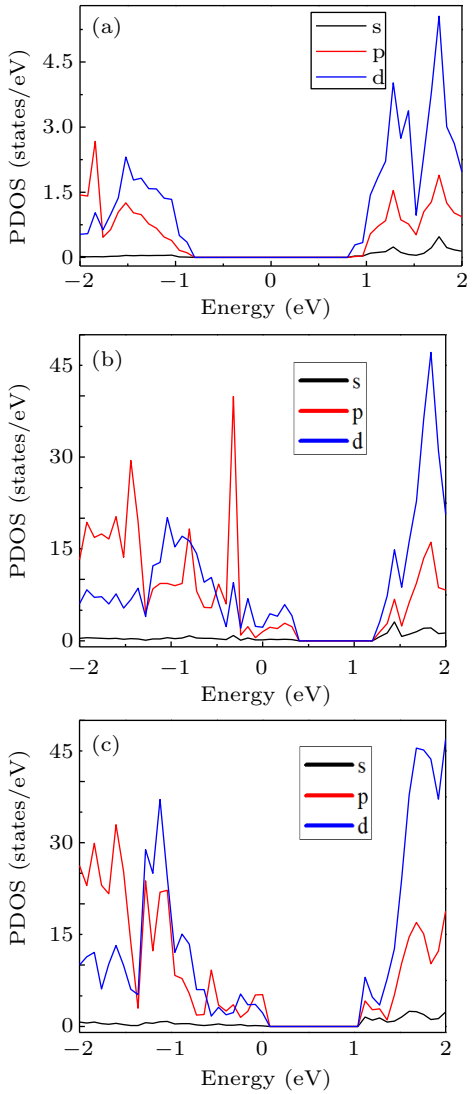



**Fig. 4.** Projected densities of states (PDOSs) for pristine and Ga-substituted systems: (a) original cell, (b) Ga-substituted zigzag configuration, (c) Ga-substituted armchair configuration. The three curves correspond to the s (black line), p (red line), and d (blue line) orbital densities of states based on the electronic localized landscape projection.

Ga doping induces newly localized impurity states within the valence and conduction band regions. Such Ga-dominated localized states hybridize strongly with the surrounding W and Se orbitals, optimizing the band structure and carrier distribution, facilitating the separation and migration of photogenerated electron–hole pairs, and consequently improving the photocurrent response intensity. Furthermore, comparative analysis among W-vacancy, Se-vacancy, S-substituted Se, and Ga-doping configurations demonstrates that only Ga doping achieves a prominent enhancement of maximum photocurrent together with improved polarization sensitivity. Although vacancy defects can introduce localized states, they easily act as carrier recombination centers and suppress photocurrent generation. S substitution can slightly adjust the band edge position, whereas its capability in tuning the Fermi level and strengthening orbital hybridization is much weaker than that of Ga doping. Consequently, the synergistic effects of a Fermi level shift, localized impurity state formation, and orbital hybridization enable Ga doping to achieve optimal electronic structure modulation, thereby realizing a substantial improvement in photocurrent and polarization performance.

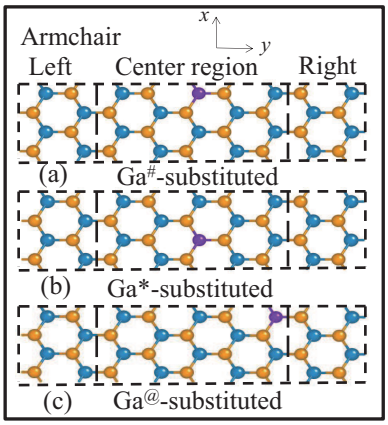



**Fig. 5.** Top view of the monolayer $WSe_2$ photodetector in the armchair direction. The blue, orange, and purple spheres represent W, Se, and Ga atoms, respectively. The defective supercells are Ga-substituted in the armchair devices. (a) 'Ga$^{\#}$-substituted' denotes a central defect where the defect is located at the top of the central region; (b) 'Ga*-substituted' denotes a central defect where the defect is located in the middle of the central region; and (c) 'Ga$^{@}$-substituted' denotes an edge-doped structure near the electrode.

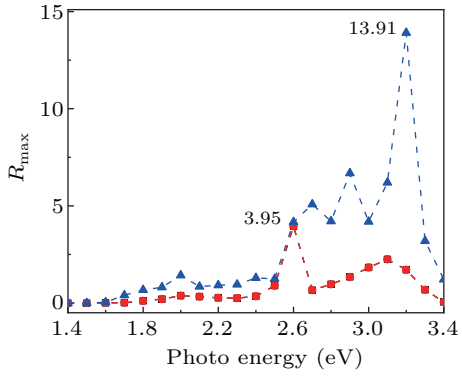



**Fig. 6.** Variation of the maximum photocurrent $R_{max}$ with defect position for the Ga-substituted material in an armchair device. The black and red lines represent central doping, while the blue line represents edge doping.

Since Ga doping exhibits the most pronounced photocurrent response along the armchair direction, this configuration is chosen to further investigate the effect of different doping sites. The blue curve in Fig. 3(b) corresponds to $R_{max}$ for central doping, which is shown as the reference data (Ga$^{\#}$) in Fig. 5(a) and as the black line in Fig. 6 for comparison with other doping sites. In Fig. 5(a), 'Ga$^{\#}$-substituted' represents a central defect where the defect is located at the top of the central region; in Fig. 5(b), 'Ga*-substituted' denotes

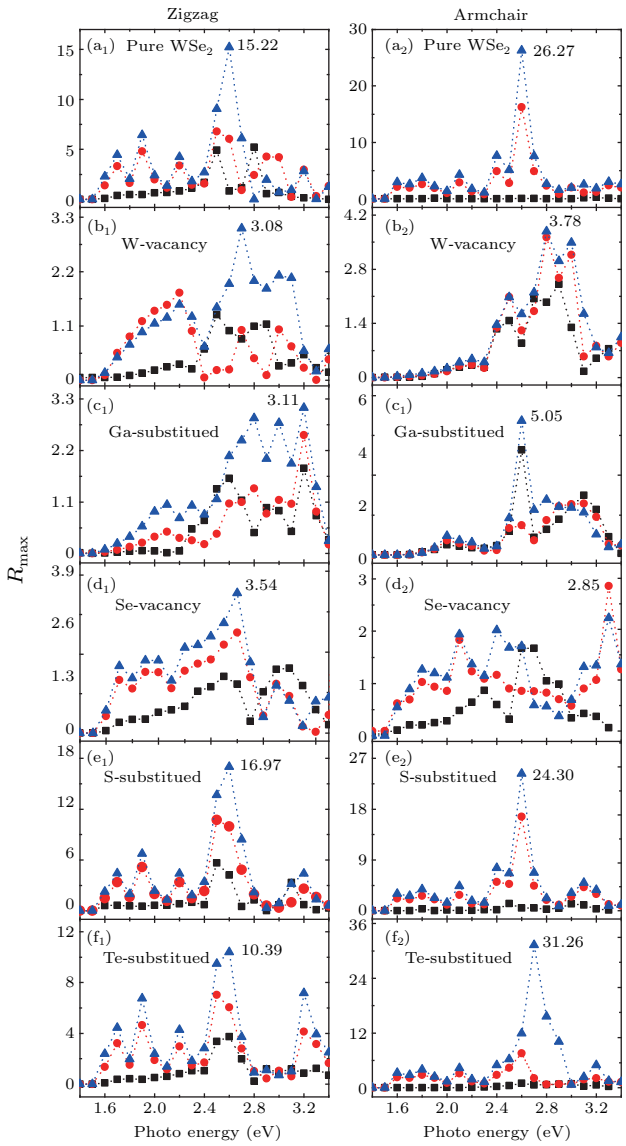



**Fig. 7.** Effect of bias voltage on maximum photocurrent $R_{max}$ in both zigzag (left column) and armchair (right column) directions for bias voltages of 0 V (black line), 0.02 V (red line), and 0.04 V (blue line). (a) Pure $WSe_2$, (b) W-vacancy, (c) Ga-substituted, (d) Se-vacancy, (e) S-substituted, and (f) Te-substituted configurations.

a central defect where the defect is located in the middle of the central region; and in Fig. 5(c), '$Ga^{@}$-substituted' denotes an edge-doped structure near the electrode. Due to the periodic structure of $WSe_2$, there is little difference between the $Ga^{*}$-substituted and $Ga^{\#}$-substituted cases, so the black line and red line coincide. In contrast, in the edge-doped case, exemplified by the $Ga^{@}$-substituted configuration (blue line in Fig. 6), $R_{max}$ reaches 13.91 at 3.2 eV, 8.1 times that of the center-doped cases, because edge states strongly break local symmetry and boost transition efficiency. A noticeable difference in $R_{max}$ between the edge-doped and center-doped samples is also observed in the low-energy region (1.4 eV–2.2 eV). However, the magnitude of this difference is relatively small, as it is far less pronounced than that in the high-energy region. It can be seen that changing the doping position affects the symmetry of the structure, thus affecting the size of the photocurrent. We conclude that when the generation of defects is unavoidable, the armchair-direction photocurrent is preferable for the manufacture of optoelectronic devices.

Figure 7 illustrates the influence of bias voltage (0 V, 0.02 V, and 0.04 V) on the $R_{max}$ values achieved by six configurations (pure $WSe_2$, W-vacancy, Ga-substituted, Se-vacancy, S-substituted, and Te-substituted) in both the zigzag (left column) and armchair (right column) directions; all bias calculations are Poisson-NEGF self-consistent. Weak bias generally enhances the photocurrent across most visible-light ranges, with striking amplification effects observed in specific cases: at 2.6 eV, pure $WSe_2$ with a bias of 0.04 V exhibits an increase of 368.90 times in $R_{max}$ compared to the $R_{max}$ observed at zero bias (Fig. 7($a_2$)); S-substituted $WSe_2$ shows a $R_{max}$ enhancement of 46.62 times at the same photon energy and bias (Fig. 7($e_2$)); and Te-substituted $WSe_2$ achieves a $R_{max}$ increase of 49.70 times at 2.7 eV with a bias of 0.04 V (Fig. 7($f_2$)). Only isolated exceptions exist, such as a reduced photocurrent at 2.8 eV for pure $WSe_2$ under bias (Fig. 7($a_1$)). Notably, the degree of amplification varies with structure and orientation. For pure $WSe_2$, zigzag devices outperform armchair devices at zero bias, but this trend reverses under bias — at 2.6 eV with a 0.04 V bias, armchair devices show higher $R_{max}$ (26.27 vs. 15.22 in the zigzag direction; see Figs. 7($a_1$) and ($a_2$)). This directional shift holds for most configurations except Se-vacancy, arising from $WSe_2$'s structural anisotropy, which modulates carrier transport and bias-dependent photoresponse differently along zigzag and armchair axes.

## 4. Extinction ratio

The photocurrent is related to the helicity $\varphi$, as shown in Fig. 2; thus, a polarized photodetector can be developed, and its sensitivity can be defined using the extinction ratio (ER), denoted by $R_{\parallel}/R_{\perp}$ (black line) or $R_{\perp}/R_{\parallel}$ (red line), where $R_{\parallel}$ and $R_{\perp}$ are the photocurrents at $\varphi = 0°$ and $\varphi = 90°$, respectively. Figure 8 shows the changes in ER with photon energy in zigzag (left column) and armchair (right column) devices. As can be seen, in zigzag devices, the maximum ER value is 23.99 when the photon energy is 2.5 eV for pure $WSe_2$ (Fig. 8($a_1$)). For photodetectors with the W-vacancy (Fig. 8($b_1$)), Ga-substituted (Fig. 8($c_1$)), Se-vacancy (Fig. 8($d_1$)), S-substituted (Fig. 8($e_1$)), and Te-substituted (Fig. 8($f_1$)) configurations, the maximum ERs are 21.24 at 1.9 eV, 178.16 at 2.6 eV, 75.44 at 3.2 eV, 30.15 at 2.1 eV, and 21.59 at 2.7 eV, respectively. In armchair devices, the maximum ER value is 8.99 in pure $WSe_2$ when the photon energy is 1.6 eV (Fig. 8($a_2$)). For photodetectors with the W-vacancy (Fig. 8($b_2$)), Ga-substituted (Fig. 8($c_2$)), Se-vacancy (Fig. 8($d_2$)), S-substituted (Fig. 8($e_2$)), and Te-substituted (Fig. 8($f_2$)) configurations, the maximum ERs are 9.17 at 1.4 eV, 416.03 at 2.2 eV, 57.70 at 3.2 eV, 4.64 at 1.6 eV, and

46.03 at 2.7 eV, respectively. It can be seen that doping generally enhances the ERs of $WSe_2$ polarized photodetectors, except in the case of S substitution in armchair devices. Appropriate Ga substitution stands out as the most effective approach — achieving maximum ERs of 178.16 (zigzag) and 416.03 (armchair), with armchair devices showing a higher peak ER than zigzag ones. These results confirm that defect engineering is a viable strategy for boosting the polarization sensitivity of PGE-driven $WSe_2$ photodetectors.

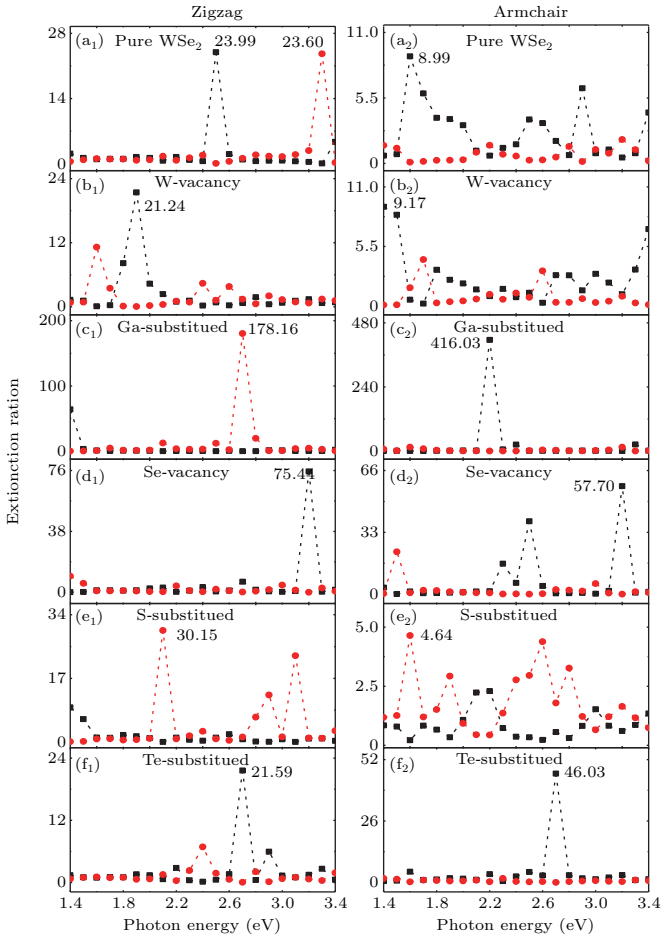



**Fig. 8.** Variation of the ER of the photocurrent with photon energy for six different central regions in zigzag (left column) and armchair (right column) devices: ($a_1$), ($a_2$) pure $WSe_2$; ($b_1$), ($b_2$) W-vacancy; ($c_1$), ($c_2$) Ga-substituted; ($d_1$), ($d_2$) Se-vacancy; ($e_1$), ($e_2$) S-substituted; and ($f_1$), ($f_2$) Te-substituted configurations. Key: $R_{\parallel}/R_{\perp}$ — black line; $R_{\perp}/R_{\parallel}$ — red line.

## 5. Conclusion

In this work, we employed quantum transport simulations combined with the NEGF formalism and DFT to systematically investigate the elliptical PGE in monolayer $WSe_2$ under elliptically polarized light irradiation. The study considered various defect types (vacancies and substitutions), transport directions (zigzag and armchair), photon energies, light helicities, and external bias voltages.

Our results demonstrate that the photocurrent exhibits strong anisotropy between zigzag and armchair directions. Defect-induced symmetry breaking from $D_{3h}$ to $C_s$ and $C_{2v}$ produces direction-dependent sinusoidal/cosine photoresponses. In zigzag-oriented devices, the photoresponse follows a sine dependence on the light helicity angle, with the maximum photocurrent occurring under circular polarization. In contrast, armchair-oriented devices exhibit a cosine dependence. Among the defect configurations, S substitution in the zigzag direction yields the highest photocurrent (5.63 at 2.5 eV), while Ga substitution in the armchair direction shows the most significant enhancement (3.95 at 2.6 eV), exceeding the photocurrent generated by the pristine structure by a factor of 55.54 due to the resonant enhancement via impurity states introduced by Ga doping. The position of defects was also found to influence the magnitude of the photocurrent by modifying structural symmetry. The application of a small bias voltage (up to 0.04 V) markedly enhanced the photocurrent across the visible spectrum, despite occasional reductions at specific photon energies. Furthermore, the introduction of defects generally increased the polarization sensitivity, with Ga substitution achieving the highest ERs in both transport directions. These findings provide valuable insights into the tunability of PGEs in 2D materials via defect engineering and symmetry breaking. The high polarization sensitivity and bias-enhanced photoresponse suggest that defect-modified $WSe_2$ monolayers — particularly those modified via Ga substitution — are promising candidates for the development of high-performance polarization-sensitive photodetectors and efficient solar energy conversion devices. These results provide guidance for the design of high-performance polarization-sensitive photodetectors.

## Acknowledgments

Project supported by the National Key Research and Development Program of China (Grant Nos. 2021YFA1400900, 2021YFA0718300, 2024YFF0726700, 12174461, 12234012, 12334012, and 52327808), the National Natural Science Foundation of China (Grant Nos. 12264037 and 12265022), the Natural Science Foundation of Inner Mongolia Autonomous Region of China (Grant Nos. 2025JQ007 and 2025LHMS01006), the Program for Young Talents in Science and Technology in Universities of Inner Mongolia Autonomous Region (Grant No. NJYT25031), the Fundamental Research Funds for Inner Mongolia University of Science, Technology (Grant No. 2023RCTD015), the China Scholarship Council (Grant No. 202308150117), the Elite Revitalizing Inner Mongolia Program (Grant No. 2025TGL05), and the Space Application System of the China Manned Space Program.

The authors thank HZWTECH for providing computation facilities.

## References


[1] Moayed M M R, Li F, Beck B, Schober J C and Klinke C 2020 *Nanoscale* **12** 6256
[2] Ganichev S D, Ketterl H, Prettl W, Ivchenko E L and Vorobjev L E 2000 *Appl. Phys. Lett.* **77** 3146
[3] Chu F, Chen M, Wang Y, Xie Y, Liu B, Yang Y, An X and Zhang Y 2018 *J. Mater. Chem. C* **6** 2509
[4] Von Baltz R and Kraut W 1981 *Phys. Rev. B* **23** 5590
[5] Ma H, Jiang C Y, Liu Y, Zhu L P, Qin X D and Chen Y H 2013 *Appl. Phys. Lett.* **102** 232402
[6] Parto K, Azzam S I, Banerjee K and Moody G 2021 *Nat. Comm.* **12** 1
[7] Guo W Q, Xu H J, Sun F P, Liu Y, Ma Y, Liu W, Zhao Y, Sun Z H and Luo J H 2025 *Angew. Chem. Int. Ed* **18** e202421463
[8] Briscoe J and Shi 2025 *J. Nat. Rev. Phys.* **5** 270
[9] Ganichev S D, Ivchenko E L, Danilov S N, Eroms J, Wegscheider W, Weiss D and Prettl W 2001 *Phys. Rev. Lett.* **86** 4358
[10] Ganichev S D, Ivchenko E L and Prettl W 2002 *Physica E* **14** 166
[11] Tang Y C, Wang Z, Wang P, Wu F, Wang Y M, Chen Y F, Wang H L, Peng M, Shan C X, Zhu Z H, Qin S Q and Hu W D 2019 *Small* **15** 1805545
[12] Huang H L, Wang D J, Zhang H R, Zhang H, Xiong C M, Sun J R and Shen B G 2017 *Chin. Phys. B* **26** 077302
[13] Cheng K, Guo Y, Han N N, Jiang X, Zhang J F, Ahuja R, Su Y and Zhao J J 2018 *Appl. Phys. Lett.* **112** 143902
[14] Shockley W 1949 *Bell Syst. Tech. J.* **28** 435
[15] He X W, Shen B, Chen Y H, Zhang Q, Han K, Yin C M, Tang N, Xu F J, Tang C G and Yang Z J 2008 *Phys. Rev. Lett.* **101** 147402
[16] Wang S H, Zhang H, Zhang J, Li S Q, Luo D B, Wang J Y, Jin K X and Sun J R 2022 *Phys. Rev. Lett.* **128** 187401
[17] Danilov S N, Golub L E, Mayer T, Beer A, Binder S, Monch E, Minar J, Kronseder M, Back C H and Bougeard D 2021 *Phys. Rev. Appl.* **21** 064030
[18] Golub L E, Ivchenko E L and Spivak B 2020 *Phys. Rev. B* **102** 085202
[19] Lai W X, Ma Y Q, Zhuang L and Liu W M 2019 *Phys. Rev. Lett.* **122** 223202
[20] Ganichev S D 2008 *Int. J. Mod. Phys. B* **22** 115
[21] Bel'kov V V, Ganichev S D, Schneider P, Back C, Oestreich M, Rudolph J, Hagele D, Golub L E, Wegscheider W and Prettl W 2003 *Solid State Commun.* **128** 283
[22] Huang P, Taniguchi K, Shigefuji M, Kobayashi T, Matsubara M, Sasagawa T and Miyasaka H 2021 *Adv. Mater.* **33** 2008611
[23] Durnev M V and Tarasenko S A 2019 *Ann. Phy.* **531** 1800418
[24] Sun X, Adamo G, Eginligil M, Krishnamoorthy H N S, Zheludev N I and Soci C 2021 *Sci. Adv.* **7** 5748
[25] De Juan F, Grushin A G, Morimoto T and Moore J E 2017 *Nat. Comm.* **8** 15995
[26] Zhang Y, Ishizuka H, van den Brink J, Felser C, Yan B H and Nagaosa N 2018 *Phys. Rev. B* **97** 241118
[27] Sun K, Sun S S, Wei L L, Guo C, Tian H F, Chen G F, Yang H X and Li J Q 2018 *Chin. Phys. Lett.* **34** 117203
[28] Manzeli S, Ovchinnikov D, Pasquier D, Yazyev O V and Kis A 2017 *Nat. Rev. Mater.* **2** 17033
[29] Zhao X G, Shi Z M, Wang X J, Zou H S, Fu Y H and Zhang L J 2021 *InfoMat* **3** 201
[30] Dias A C, Qu F Y, Azevedo D L and Fu J 2018 *Phys. Rev. B* **98** 075202
[31] Li H, Wu J, Yin Z Y and Zhang H 2014 *Accounts Chem. Res.* **47** 1067
[32] Tan L L, Liu Q B, Ding Y F, Lin X G, Hu W, Cai M Q and Zhou H 2020 *Nano Res.* **13** 557
[33] Wang H R, Sun Z X, Wei Z S and Wu Y Y 2022 *Nanomaterials* **12** 1784
[34] Li H, Lu G, Wang Y L, Yin Z Y, Cong C X, He Q Y, Wang L, Ding F, Yu T and Zhang H 2013 *Small* **9** 1974
[35] Liu N, Kim P, Kim J H, Ye J H, Kim S and Lee C J 2014 *ACS Nano.* **8** 6902
[36] Zheng J, Zhang H, Dong S H, Liu Y P, Nai C T, Shin H S, Jeong H Y, Liu B and Loh K P 2014 *Nat. Comm.* **5** 1
[37] Lv R, Robinson J A, Schaak R E, Sun D, Sun Y F, Mallouk T E and Terrones M 2014 *Accounts Chem. Res.* **48** 56
[38] Chhowalla M, Shin H S, Eda G, Li L J, Loh K P and Zhang H 2013 *Nat. Chem.* **5** 263
[39] Tongay S, Zhou J, Ataca C, Lo K, Matthews T S, Li J B, Grossman J C and Wu J Q 2012 *Nano Lett.* **12** 5576
[40] Li H, Qi X Y, Wu J, Zeng Z Y, Wei J and Zhang H 2013 *ACS Nano* **7** 2842
[41] Yuan H, Wang X, Lian B, Zhang H, Fang X, Shen B, Xu G, Xu Y, Zhang S C and Hwang H Y 2014 *Nat. Nanotech.* **9** 851
[42] Xu Z H, Chen Z and Yuan Q M 2021 *Physica E* **133** 114846
[43] Yang B Y, Zhang J M, Ali A, Huang Y H and Wei X M 2021 *Thin Solid Films.* **732** 138793
[44] Liu Y, Zhou J Y, Xu L, Long J, Cheng Q and Zeng W 2022 *J. Mater. Res. Tech.* **17** 1786
[45] Sun X X, Yin S Q, Wei D, Li Y, Ma Y Q and Dai X Q 2023 *Appl. Surf. Sci.* **610** 155401
[46] Chowdhury S, Venkateswaran P and Somvanshi D 2022 *Europhys. Lett.* **137** 26004
[47] Wu J H, Zhai F, Lu J Q, Wu J and Feng X 2020 *Mater. Today Comm.* **24** 101154
[48] Taylor J, Guo H and Wang J 2001 *Phys. Rev. B* **63** 245407
[49] Liu J, Ma Y H, Chi F, Chao L M and Niu J Y 2023 *Opt. Express* **31** 12026
[50] Liu P P, Shao Z G, Luo W M and Yang M 2021 *Physica E* **128** 114577